PHOTONICS Research

Transient long-range distance measurement by a Vernier spectral interferometry

Liang Xu,[1,2] Kun Wang,[1,2] Chen Liu,[1,2] Wenying Chen,[1,2] Chi Zhang,[1,2,*] AND Xinliang Zhang[1,2]

[1]*Wuhan National Laboratory for Optoelectronics, Huazhong University of Science and Technology, Wuhan 430074, China*
[2]*Optics Valley Laboratory, Wuhan 430074, China*
*Corresponding author: chizheung@hust.edu.cn

Rapid and long-range distance measurements are essential in various industrial and scientific applications, and among them, the dual-comb ranging system attracts great attention due to its high precision. However, the temporal asynchronous sampling results in the tradeoff between frame rate and ranging precision, and the non-ambiguity range (NAR) is also limited by the comb cycle, which hinders the further advancement of the dual-comb ranging system. Given this constraint, we introduce a Vernier spectral interferometry to improve the frame rate and NAR of the ranging system. First, leveraging the dispersive time-stretch technology, the dual-comb interferometry becomes spectral interferometry. Thus, the asynchronous time step is unlimited, and the frame rate is improved to 100 kHz. Second, dual-wavelength bands are introduced to implement a Vernier spectral interferometry, whose NAR is enlarged from 1.5 m to 1.5 km. Moreover, this fast and long-range system also demonstrated high precision, with a 22.91-nm Allan deviation over 10-ms averaging time. As a result, the proposed Vernier spectral interferometry ranging system is promising for diverse applications that necessitate rapid and extensive distance measurement.   © 2024 Chinese Laser Press

https://doi.org/10.1364/PRJ.515112

1. INTRODUCTION

Long-range distance measurement is crucial in scientific and industrial fields, such as multi-satellite flight formation missions, large-scale manufacturing, and autopilot. In these applications, laser-based light detection and ranging (LiDAR) technology is always appealing because it provides the ranging system with long range, high precision, and frame rate, enabling real-time tracking of the relative positions of individual samples [1–4]. In the conventional LiDAR system, an interferometer is introduced to acquire the interferometric phase of a continuous wave, and sub-wavelength precision is achieved [5,6]. However, its non-ambiguity range (NAR) is confined to half of the wavelength. Although multi-wavelength or synthetic wavelength interferometry has been proposed to increase NAR [7–13], the phase stability between each wavelength hinders its applications [14–16]. Alternatively, radio-frequency-modulated waveforms or pulsed light sources have also been applied to adjust the trade-off between NAR and precision, and extended NAR resulted in poor precision [17–19].

The advent of optical frequency combs (OFCs), which feature broadband coherent light sources, has revolutionized absolute distance measurements [20–26]. Benefitting from equidistant modes and ultrashort pulses, ranging approaches based on spectral interferometry [27–31] or time-of-flight (TOF) [32,33] have been demonstrated with advanced precision and NAR. Spectral interferometry generally exhibits better precision, while the spectrometer's resolution constrains NAR. On the other hand, TOF is a straightforward way to measure distance and is easier to achieve large NAR, while its precision is restricted by the electrical bandwidth of the photodetectors [34,35]. To overcome the bandwidth limit, an asynchronous dual-comb with slightly different repetition rates (f_{rep1}, f_{rep2}) was introduced [36–40]. Instead of direct detection, the TOF pulse is optically sampled by the other asynchronous comb, with an effective time step $\Delta T_r = |f_{rep1} - f_{rep2}|/(f_{rep1}f_{rep2})$, and it offers high precision for absolute distance measurement. However, the Nyquist sampling theorem requires the time step to be less than the inverse of the comb bandwidth, which slows down the frame rate [41,42].

In this study, we present a dual-comb-based Vernier spectral interferometry for transient long-range distance measurement. Adopting dispersive time-stretch technology, the intrinsic constraint on the frame rate imposed by the Nyquist sampling theorem is eliminated. Furthermore, the NAR has been advanced to 1.5 km with the Vernier-based dual-wavelength-band scheme. As a proof-of-concept demonstration, a stationary target at approximately 420-m distance is successfully characterized with a 100-kHz frame rate, and the variance of fluctuations is within ±5 μm. If accumulating frames over 10 ms, the ranging precision can be improved to 23 nm.

This Vernier spectral interferometry is promising for further applications where the long-distance information is utilized within a feedback system to orient the components in real time.

2. PRINCIPLE

A. Frame Rate Enhancement by Time-Stretch-Based Spectral Interferometry

As depicted in Figs. 1(a) and 1(b), the pulse train originating from the signal comb source undergoes reflection when encountering both a sample and a reference. The TOF is then determined by heterodyning reflections against a local oscillator comb. The frame rate $\Delta f_{\mathrm{rep}} = |f_{\mathrm{rep1}} - f_{\mathrm{rep2}}|$ is commonly constrained to prevent under-sampling of the pulses. A time-stretch-based spectral interferometry is proposed and demonstrated to overcome the limitation.

Ignoring the amplitude and carrier frequency, the electrical field of a Gaussian pulse can be formulated as $E_0(t) = \exp[-2 \ln 2(t/\tau_{\mathrm{pw}})^2]$, where τ_{pw} denotes the full width at half maximum pulse width. In addition, the transfer function of the dispersion fiber can be expressed as $D(\omega) = \exp(-i\Phi_0\omega^2/2)$, where Φ_0 represents the total group delay dispersion (GDD). Therefore, the time-stretched pulse can be expressed as

$$E_s(t) = \mathcal{F}^{-1}\{\mathcal{F}[E_0(t)] \cdot D(\omega)\} \approx \sqrt{\frac{1}{iM}}$$
$$\cdot \exp\left[-2 \ln 2\left(\frac{t}{M\tau_{\mathrm{pw}}}\right)^2\right] \cdot \exp\left(i\frac{t^2}{2\Phi_0}\right)$$
$$= A_s(t) \cdot \exp\left(i\frac{t^2}{2\Phi_0}\right), \tag{1}$$

where $\mathcal{F}$ and $\mathcal{F}^{-1}$ denote the Fourier transform and inverse Fourier transform, respectively. The time-domain far-field diffraction condition $(4 \ln 2 \cdot \Phi_0 \gg \tau_{\mathrm{pw}}^2)$ is considered [43], and $M = 4 \ln 2 \cdot \Phi_0/\tau_{\mathrm{pw}}^2 \gg 1$ is the magnification factor of the pulse width. Since the pulse width is significantly broadened, pulses from the reference will interfere with the local arm, leading to frequency-varied fringes. This can be expressed as

$$I_{\mathrm{ref}}(t) = |E_{\mathrm{loc}}(t) + E_{\mathrm{ref}}(t)|^2$$
$$= \sum_{n=-\infty}^{+\infty} \left|E_s\left(t - \frac{n}{f_{\mathrm{rep1}}}\right) + E_s\left(t - \frac{n}{f_{\mathrm{rep2}}} - \tau_{\mathrm{ref}}\right)\right|^2$$
$$= 2\sum_{n=-\infty}^{+\infty} A_s^2\left(t - \frac{n}{f_{\mathrm{rep1}}}\right)\left\{1 + \cos\left[\frac{\tau_{\mathrm{ref}} - n\Delta T_r}{\Phi_0}t - \phi_{\mathrm{ref}}(n)\right]\right\}, \tag{2}$$

where τ_{ref} denotes the temporal delay introduced by the optical path difference (OPD) between the local and reference arms. Since the relative time offset between the adjacent pairs of pulses proceeds at a constant increment of ΔT_r, it is feasible to ascertain this time offset by resolving solely the central two interferometric fringes. An acquisition bandwidth limitation denoted by $f_0 = \Delta T_r/(2\pi\Phi_0)$ can be adopted, enabling the exclusion of the high-frequency components, and only the two central frames are obtained and considered reference fringes. It corresponds to $n = n_1$ and n_2, two neighboring frames whose frequencies are f_{r1} and f_{r2}. Therefore, the temporal delay of the reference arm should be $\tau_{\mathrm{ref}} = 2\pi\Phi_0 f_{r1} + n_1\Delta T_r = -2\pi\Phi_0 f_{r2} + n_2\Delta T_r$, where $f_{r1} + f_{r2} = f_0$. Considering the sample-induced delay τ_{sample}, the sample fringes reflected from the sample and local arms can be expressed as

$$I_{\mathrm{sample}}(t) = |E_{\mathrm{loc}}(t) + E_{\mathrm{sample}}(t)|^2$$
$$= \sum_{m=-\infty}^{+\infty} \left|E_s\left(t - \frac{m}{f_{\mathrm{rep1}}}\right) + E_s\left(t - \frac{m}{f_{\mathrm{rep2}}} - \tau_{\mathrm{sample}}\right)\right|^2$$
$$= 2\sum_{m=-\infty}^{+\infty} A_s^2\left(t - \frac{m}{f_{\mathrm{rep1}}}\right)$$
$$\times \left\{1 + \cos\left[\frac{\tau_{\mathrm{sample}} - m\Delta T_r}{\Phi_0}t - \phi_{\mathrm{sample}}(m)\right]\right\}. \tag{3}$$

Similarly, the fringes of the two neighboring frames corresponding to $m = m_1$ and m_2 are obtained, and the frequency is f_{s1} and f_{s2}. The temporal delay of the sample arm should be $\tau_{\mathrm{sample}} = 2\pi\Phi_0 f_{s1} + m_1\Delta T_r = -2\pi\Phi_0 f_{s2} + m_2\Delta T_r$, where
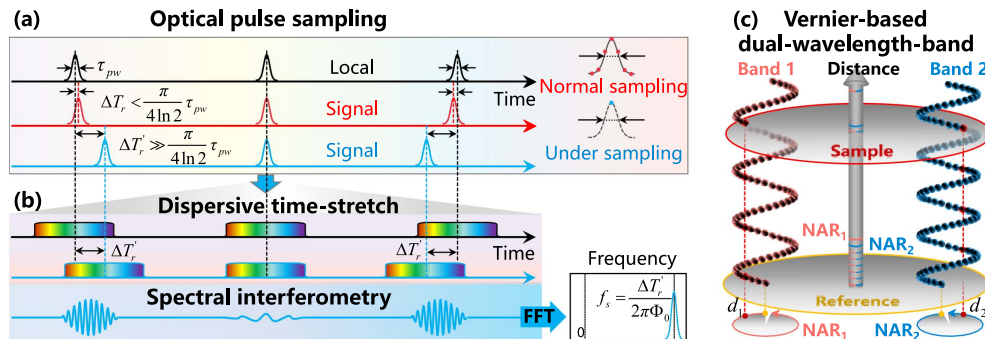

Fig. 1. Concept of the Vernier spectral interferometry. (a) Optical pulse sampling in conventional dual-comb method. The relative timing between the local (black) and signal (red or blue) pulses proceeds in increments of ΔT_r with each sequential pulse. The ΔT_r should satisfy the Nyquist sampling theorem, otherwise resulting in under-sampling. (b) After the dispersive time-stretch, the broadened pulses of the local (black) and signal (blue) interact, leading to frequency-varied fringes. The dual-comb interferometry converts into spectral interferometry. (c) Circular mapping of sample distance (the plane spacing marked by the yellow and red circles) to the measured results (d_1, d_2). Measured results do not exceed the NAR of the two bands.

$f_{s1} + f_{s2} = f_0$. Therefore, the absolute sample distance over the reference arm can be expressed as

$$D_{\text{sample}} = \frac{v_g}{2}(\tau_{\text{sample}} - \tau_{\text{ref}})$$
$$= \frac{v_g}{2}[2\pi\Phi_0 \cdot (f_{s1} - f_{r1}) + (m_1 - n_1)\Delta T_r], \quad (4)$$

where v_g represents the group velocity and D_{sample} denotes the OPD between the sample and reference arms. The temporal delay to be measured can be written as $\tau_{\text{sample}} - \tau_{\text{ref}} = \Delta n \cdot \Delta T_r + 2\pi\Phi_0(f_{s1} - f_{r1})$, where $\Delta n = m_1 - n_1$ is an integer, and $f_{s1} - f_{r1}$ can be derived from the reference and sample fringes in the n_1^{th} and m_1^{th} periods.

B. NAR Extension by Vernier Spectral Interferometry

Due to the periodicity of the pulses, the NAR is confined to the repetition rate of the utilized signal comb, and it can be written as $\text{NAR} = v_g/2f_{\text{rep}}$. The sample distance can be expressed as

$$D_{\text{sample}} = p \cdot \text{NAR} + d, \quad d < \text{NAR}, \quad (5)$$

where p is a positive integer to be derived, and d is the sample distance modulo the NAR. As shown in Fig. 1(c), the sample distance D_{sample} that exceeds the NAR will be mapped into a wrapped result. In this research, we conduct a concurrent measuring for NAR extension by adopting a Vernier-based dual-wavelength-band scheme, with $\text{NAR}_1 = v_g/2f_{\text{rep1}}$ and $\text{NAR}_2 = v_g/2f_{\text{rep2}}$. Therefore, the sample distance can be given by $D_{\text{sample}} = p_1 \cdot \text{NAR}_1 + d_1 = p_2 \cdot \text{NAR}_2 + d_2$. Since NAR_1 and NAR_2 have slight differences, p_1 and p_2 should be equal or spaced by one, and can be calculated as

$$\begin{cases} p_1 = \text{round}\left(\frac{d_2 - d_1}{\text{NAR}_1 - \text{NAR}_2}\right), & \text{if } d_2 - d_1 \geq 0 \ (p_2 = p_1), \\ p_1 = \text{round}\left(\frac{d_2 + \text{NAR}_2 - d_1}{\text{NAR}_1 - \text{NAR}_2}\right), & \text{if } d_2 - d_1 < 0 \ (p_2 = p_1 + 1), \end{cases}$$
$$(6)$$

where round refers to the nearest integer, and the value of p_1 is subject to an upper limit, represented as $p_{1,\text{max}}$ when the accumulated difference between the two NARs covers NAR_2. It can be expressed as

$$p_{1,\text{max}} = \frac{\text{NAR}_2}{\text{NAR}_1 - \text{NAR}_2}. \quad (7)$$

As a consequence, the enlarged NAR for the system is determined by the repetition rate difference:

$$\text{NAR}_{\text{dual-probe}} = p_{1,\text{max}} \cdot \text{NAR}_1 = \frac{\text{NAR}_1 \cdot \text{NAR}_2}{\text{NAR}_1 - \text{NAR}_2} = \frac{v_g}{2\Delta f_{\text{rep}}}. \quad (8)$$

It is noticed that the NAR has evolved from being determined by the repetition rate to the repetition rate difference related, which is upgraded by three orders of magnitude in this work. Compared with other technologies for NAR extension, such as adjusting repetition rate or adding an extra measurement path, the Vernier-based dual-wavelength-band method offers real-time measuring capabilities and significantly simplifies the measurement process.

3. EXPERIMENTAL SETUP

Figure 2 illustrates the experimental setup of the ranging system. The dual-comb, operating at a repetition rate of 100 MHz and a repetition rate difference of 100 kHz, has been synchronized to a reference clock (R&S SMU200A) using a digital phase-locked loop (DPLL). Dual-comb sources are introduced into a dispersion module comprising a spool of dispersion compensation fiber (DCF) and large effective area fiber (LEAF). This leads to a group delay dispersion of approximately 497 ps^2. Implementing the LEAF aims to mitigate the impact of high-order dispersion in DCF, especially third-order dispersion. The wavelength division multiplexer coupler (WDMC) configures the time-stretched pulses into two branches, each consisting of broadened pulses with a bandwidth of 18 nm centered at 1539 and 1558 nm. One branch functions as a probe, while the other functions as the local oscillator. In this approach, it is imperative that the two probes remain non-interacting to prevent potential confusion in the obtained results, otherwise rendering it ineffective. Given this, the probes from the dual-comb sources with distinct wavelength bands are coupled into both the sample and reference arms, as depicted in different colored pulses in Fig. 2. The
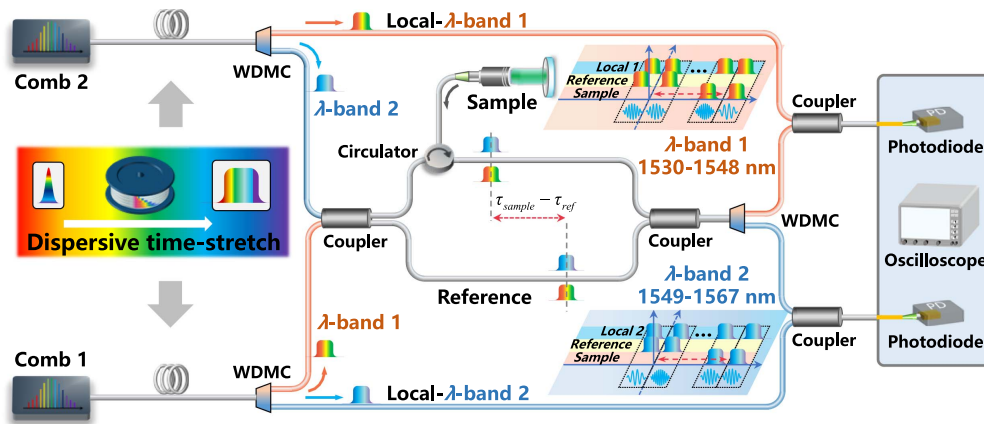
Fig. 2. Schematic of the experimental setup. Pulse trains generated from dual-comb sources are launched into a dispersion module and divided into sample and local sources by WDMC. The dual-wavelength bands are coupled into the sample and reference arms and separated to interact with local sources. The dual-wavelength-band results are captured by an acquisition module consisting of two photodiodes and one oscilloscope.
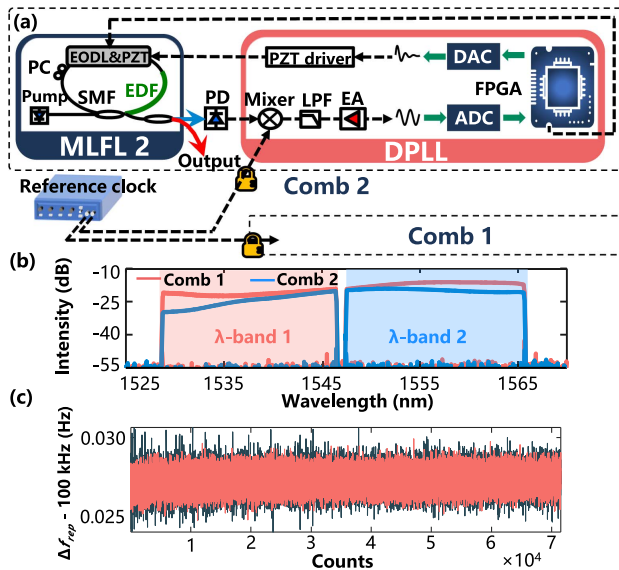
Fig. 3. (a) Schematic of mock-locked fiber laser (MLFL) and DPLL. The comb 1 possesses the same configuration as comb 2. The phase locking system is based on a two-channel FPGA platform, and it consists of electrical components, such as mixers, low-pass filters (LPFs), and electrical amplifiers (EAs). (b) The dual-comb spectra are divided into two distinct wavelength bands, λ-band 1 (red shaded area) and λ-band 2 (blue shaded area). (c) Stability of the repetition rate difference: reference clock (red) and dual-comb system (black).

dual-wavelength bands are subsequently separated by another WDMC and undergo interference with the local oscillator, which jointly experience a delay induced by the OPD between the two arms. In this manner, the dual-comb serves the dual purpose of acting as both a probe and a local source, with each probe measuring the OPD. The interferograms are obtained by

a photodiode (Finisar XPDV2120RA) and an oscilloscope (Keysight DSAZ594A).

A critical factor for the precision is the frequency stability of the comb source. Thus, the detailed DPLL is depicted in Fig. 3(a). An electronically controlled optical delay line (EODL) is employed for coarse adjustment of cavity length, while a piezoelectric transducer (PZT) is also integrated into the EODL for fine-tuning. Adjusting the EODL and PZT simultaneously for each laser can achieve a wide range of precise cavity length control, thereby locking the repetition frequency to the reference clock. The dual-wavelength-band spectrum is also shown in Fig. 3(b). The variations of Δf_{rep} were recorded by a universal frequency counter (Keysight 53230A) at time intervals of 0.1 s over about 7200-s measurement, as shown in Fig. 3(c). The standard deviation of the dual-comb system (black) is approximately 8.4×10^{-4} Hz, which approaches the value of 6.9×10^{-4} Hz of the reference clock (red), suggesting a high level of performance in frequency synchronization.

4. RESULTS

As a proof-of-principle demonstration, measurements were conducted at three distance ranges: below 1.5 mm, between 1.5 mm and 1.5 m, and beyond 1.5 m. To effectively capture signal fringes while mitigating the impact of high-frequency components, it is recommended to restrict the acquisition bandwidth to $f_0 = \Delta T_r/(2\pi\Phi_0) = 3.2$ GHz, which can be realized by using digital filtering after the photodiode and oscilloscope. Figures 4(a)–4(c) present the normalized signals, enlarged views, and their Fourier transform spectra for the three distance ranges. The Fourier transform spectra were obtained by performing the Fourier transform on each fringe individually. The red and blue signals correspond to the wavelength bands 1 and 2, respectively. The sample and reference signals overlap when the sample distance is below the asynchronous
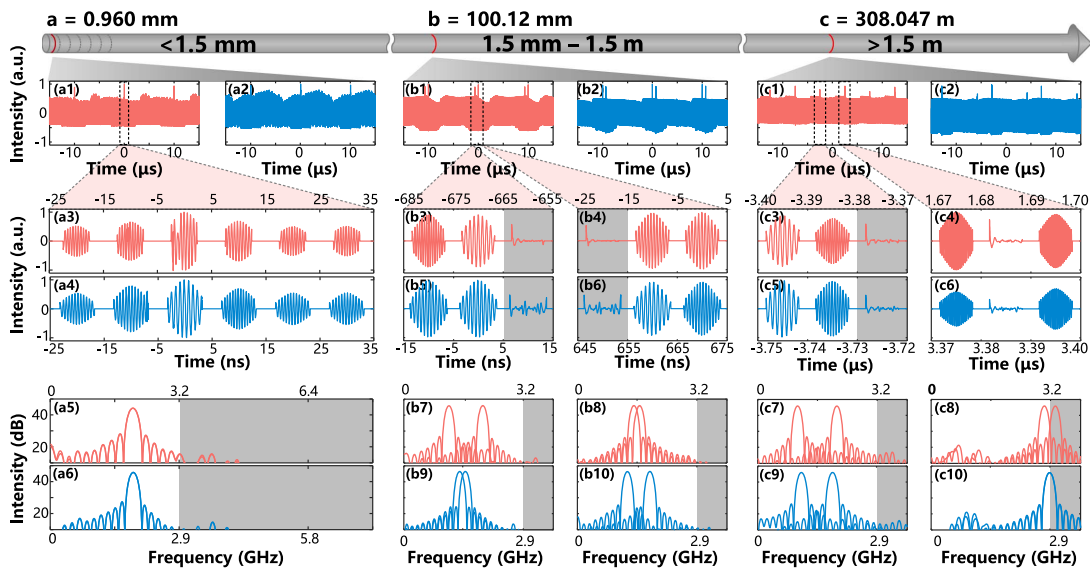

Fig. 4. Signal properties of the Vernier spectral interferometry at different locations. (a)–(c) Signals at distances of 0.960 mm, 100.12 mm, and 308.047 m, respectively. (a1), (a2) Normalized digitized signals of band 1 (red) and band 2 (blue). (a3), (a4) Enlarged views of peaks in (a1) and (a2). (a5), (a6) Fourier transform spectra of the fringes. The gray region denotes the acquisition bandwidth limitation. (b1)–(b10) Signal properties at a distance of 100.12 mm. (c1)–(c10) Signal properties at a distance of 308.047 m.
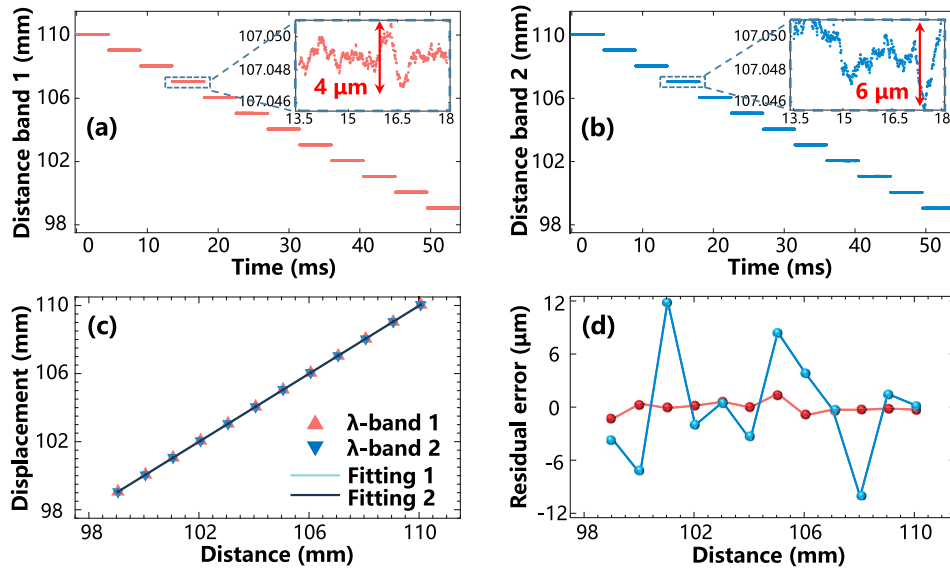
Fig. 5. Results of measuring displacement. (a), (b) Results of band 1 (marked in red) and band 2 (marked in blue). The insets show the zoom-in views of the results at a distance of 107.048 mm. (c) Averaging results and fitting lines. Results of band 1 are marked by the red triangle, while band 2 is characterized by the blue inverted triangle. (d) Residual error of the measured results and fitting line.

step: $\Delta T_r \cdot v_g / 2 = 1.5$ mm, as seen in Figs. 4(a1) and 4(a2). The homogeneous fringes presented in Figs. 4(a3) and 4(a4) arise from interference between the sample and reference arms. Figures 4(a5) and 4(a6) depict the Fourier transform spectra of dual-band signals, showcasing the point spread functions (PSFs) of signal fringes. The PSFs exhibit a minor frequency variation in Figs. 4(a5) and 4(a6) because the GDD Φ_0 for the dual-wavelength bands differs slightly. Additionally, it indicates a constant delay slide between sample and reference pulses, and the distance can be expressed as $D_{\text{sample}} = v_g \cdot \pi f \Phi_0$, where f represents the fringe frequency.

Their interference can be neglected if the distance between the sample and reference arms is beyond 1.5 mm since it exceeds the acquisition bandwidth. Two peaks are appearing in Figs. 4(b1) and 4(b2), referring to the sample and reference interference with the asynchronous local oscillator. Since $f_{\text{rep1}} < f_{\text{rep2}}$, the sample signal advances in time compared to the reference signal in Fig. 4(b1), whereas the order is reversed in Fig. 4(b2). Figures 4(b3)–4(b6) present enlarged views of two adjacent interference fringes. These fringes result from the interference between the local oscillator and the sample or reference source. Beyond these, the bandwidth exceeds the acquisition limitation, rendering it undetectable, as depicted in the gray region. The frequency between adjacent fringes denotes a time delay ΔT_r, as depicted in Figs. 4(b7)–4(b10). Consequently, the absolute sample distance can be derived from the PSFs of reference and sample signals according to Eq. (4). When the sample distance exceeds the NAR$_1$ (~ 1.5 m), the results obtained from the dual-wavelength bands exhibit dissimilarities, as shown in Figs. 4(c1)–4(c10). Based on the Vernier effect of the dual-wavelength band, the sample distance D_{sample} can be computed according to Eqs. (5) and (6). Signals in Figs. 4(c4) and 4(c6) manifest a slight oscillation during the middle period, resulting mainly from the near-zero

frequency of the middle fringes, making them difficult to detect. It is noted that a deviation may arise when the fringe frequency closely approaches the bandwidth threshold, as shown in Figs. 4(c8) and 4(c10). A slightly larger bandwidth limitation, such as a 4-GHz bandwidth, can be utilized.

We have performed a stepped distance measurement to characterize the accuracy of the ranging system. The sample mirror was mounted on a stepping motor (Newport LTA-HS), moving at a 1-mm step interval. The results, recorded by two bands, are depicted in Figs. 5(a) and 5(b). Each displacement was obtained in a 5-ms time with a sliding average time of 0.5 ms. The zoom-in views of the results at 107.048 mm reveal the maximum deviations of 4 and 6 μm, respectively. The averaging results and fitting lines are shown in Fig. 5(c), and its linearity is assessed using the Pearson correlation coefficients, which are 0.99999998 and 0.999998, indicating a high degree of linearity. Residuals can be further obtained, as shown in Fig. 5(d), and a more distinct variation in the results of band 2 may result from a more significant impact of residual high-order dispersion on long-wavelength regions.

Furthermore, the long-distance ranging capability of the Vernier spectral interferometry system has also been demonstrated. A spool of high-nonlinear dispersion-shifted fiber with near-zero dispersion was utilized to replace the mirror in the sample arm. Since the length discrepancy between the sample and reference branches exceeds the defined ambiguity range, the results are depicted in Fig. 6(a) as well. The integer value of the NAR can be estimated according to Eq. (6), as shown in Fig. 6(b). The estimated p-value is approximately 205, with a standard deviation of 6×10^{-4}, a negligible system uncertainty. For a stationary sample, the accuracy of the ultimate estimation of p can be considerably enhanced by averaging with more datasets, which takes advantage of a rapid frame rate. Thus, the fiber
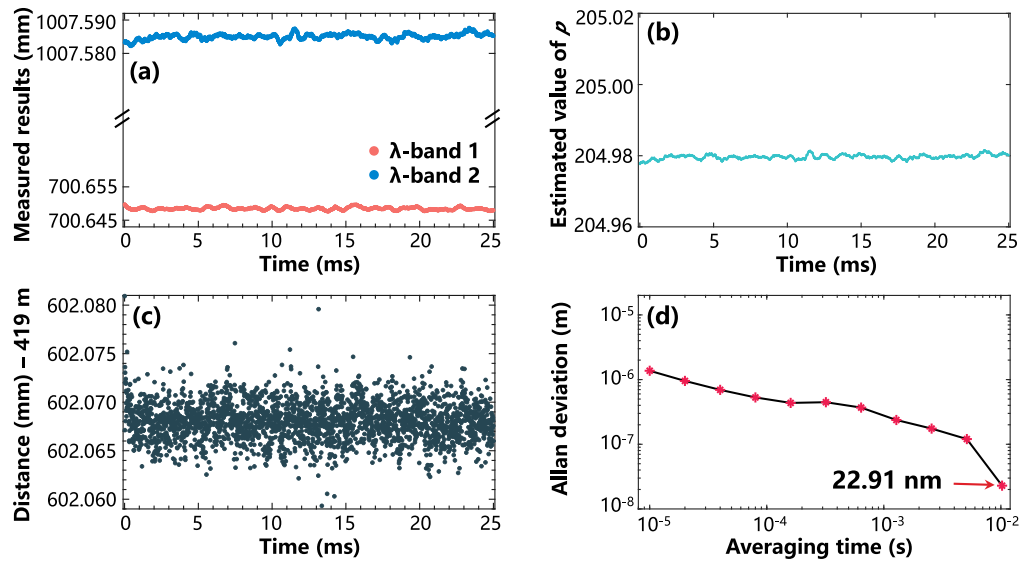
Fig. 6. Results of the stationary sample. (a) Measured results of λ-band 1 (red) and λ-band 2 (blue). (b) The estimated value of p is derived from Eq. (6). (c) Distance measurement results recovered from the two measured results in (a). (d) Allan deviation varies with averaging time.
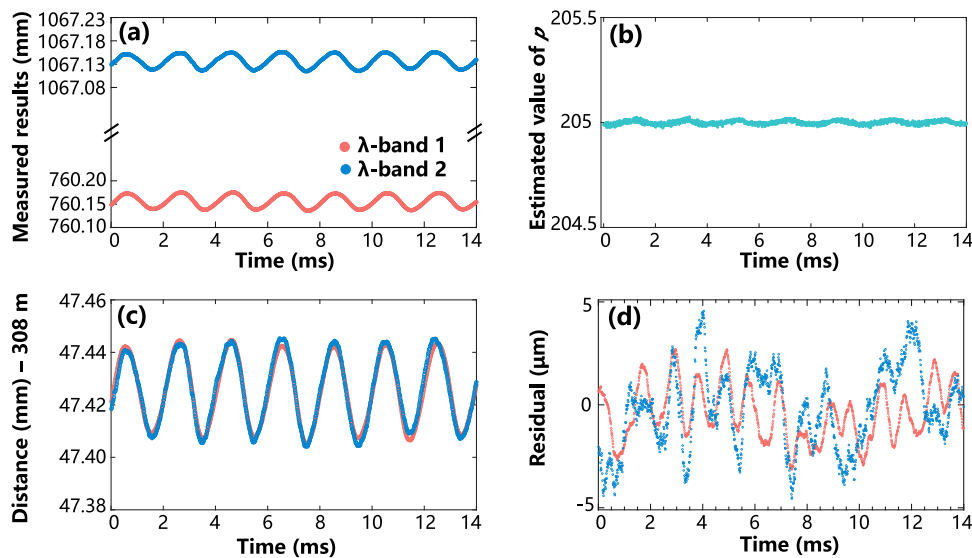

Fig. 7. Dynamic distance results. A sinusoidal voltage-driven fiber stretcher accomplishes distance variation. (a) Measured results (wrapped) of band 1 (red) and band 2 (blue). (b) Estimated value of p. (c) Retrieved traces of the distance variation. (d) Residuals of the measured results and a standard sinusoidal function.

length can be retrieved in Fig. 6(c). The time interval between two adjacent measurement results is 0.01 ms, corresponding to the 100-kHz frame rate. The distance is about 419.602 m, in good agreement with an optical time-domain reflectometry measurement (using the same group index of 1.468) of approximately 420.1 ± 1 m. The variation of the results is within ± 10 μm, which could be attributed to the slight fluctuations in the fiber group index. Figure 6(d) depicts the Allan deviations decreasing with the averaging time. The deviation reaches 22.91 nm in 10-ms averaging time.

To demonstrate the ability to measure dynamic variations in real time, we conducted distance measurements with the assistance of a long fiber. The testing configuration included a PZT-based fiber stretcher and was used to measure the elongations and frequency of sinusoidal excitations. The PZT-based fiber stretcher was driven by an amplified sinusoidal voltage at 500 Hz, generated by an arbitrary waveform generator (AWG). As depicted in Fig. 7(a), the red and blue lines represent the two results for the 14-ms time window, showing a sinusoidal trajectory. Figure 7(b) illustrates the value of the

integer p derived from Fig. 7(a). As a result, the traces are recovered in Fig. 7(c). It can be observed that the system can track the rapid displacement in real time, and the frequency is about 502 Hz after the Fourier transform is conducted on the retrieved trace. This discrepancy can be ascribed to AWG's inherent frequency deviation and the fiber stretcher's mechanical deviation. Compared with the fitting sinusoidal trace, the residuals are within ±5 μm, as shown in Fig. 7(d). It is verified that the Vernier spectral interferometry approach possesses the capability of dynamic measurements at a frame rate of 100 kHz.

5. CONCLUSION

In conclusion, we have proposed and demonstrated a novel transient long-range distance measurement approach. By integrating the dispersive time-stretch, the inherent limitation of the Nyquist sampling theorem is considerably mitigated, resulting in a high frame rate. Additionally, we performed a Vernier-based dual-wavelength-band measuring to expand the measurement range, increasing the NAR to 1.5 km. The system has demonstrated the ability to achieve a precision of 22.91 nm and a 100-kHz frame rate for long-range distance measurement. Moreover, it offers the advantage of conveniently adjustable frequency difference, enabling it to achieve a versatile frame rate and the NAR. In addition, the reduction in measurement time leads to a larger dataset of results, thereby enhancing the accuracy of the stationary sample by averaging. Benefiting from its high frame rate and large NAR, the system possesses the potential to track dynamic moving samples in real time for various applications in industrial manufacturing and scientific research. For instance, it can potentially monitor the axial clearance between the rotor and stator, a critical design parameter that directly affects major rotating machinery equipment. Achieving a frame rate of several hundred kHz for measuring the axial clearance helps to improve the efficiency and safety of rotating machines.

Last, we would like to highlight the potential for advancing the Vernier-based dual-wavelength-band method. A single-cavity dual-comb laser is also used for system simplicity and stability [44–46]. The resolution can be further improved by employing the polarization multiplexing technology to perform the Vernier-based ranging [47], allowing optimal bandwidth utilization. To achieve a frame rate exceeding 100 kHz, it is feasible to enlarge the dual-comb repetition rate difference beyond the Nyquist limit, resulting in a reduced NAR. A third comb exhibiting a slight repetition rate difference can also be utilized to extend the NAR further while the other two combs perform a rapid and refined measurement. Additionally, employing a multi-wavelength bands approach can facilitate the detection of multiple targets simultaneously.

Disclosures. The authors declare no conflicts of interest.

Data Availability. Data underlying the results presented in this paper are not publicly available at this time but may be obtained from the authors upon reasonable request.

REFERENCES

1. D. Massonnet, M. Rossi, C. Carmona, *et al.*, "The displacement field of the Landers earthquake mapped by radar interferometry," Nature **364**, 138–142 (1993).
2. M. Fridlund, "Future space missions to search for terrestrial planets," Space Sci. Rev. **135**, 355–369 (2008).
3. Y. Gong, J. Luo, and B. Wang, "Concepts and status of Chinese space gravitational wave detection projects," Nat. Astron. **5**, 881–889 (2021).
4. C. P. Hsu, B. Li, B. Solano-Rivas, *et al.*, "A review and perspective on optical phased array for automotive LiDAR," IEEE J. Sel. Top. Quantum Electron. **27**, 8300416 (2021).
5. S. Nagano, T. Yoshino, H. Kunimori, *et al.*, "Displacement measuring technique for satellite-to-satellite laser interferometer to determine earth's gravity field," Meas. Sci. Technol. **15**, 2406 (2004).
6. R. Pierce, J. Leitch, M. Stephens, *et al.*, "Intersatellite range monitoring using optical interferometry," Appl. Opt. **47**, 5007–5019 (2008).
7. G. Wu, M. Takahashi, H. Inaba, *et al.*, "Pulse-to-pulse alignment technique based on synthetic-wavelength interferometry of optical frequency combs for distance measurement," Opt. Lett. **38**, 2140–2143 (2013).
8. Y.-S. Jang, K. Lee, S. Han, *et al.*, "Absolute distance measurement with extension of nonambiguity range using the frequency comb of a femtosecond laser," Opt. Eng. **53**, 122403 (2014).
9. Z. Zhu, G. Xu, K. Ni, *et al.*, "Synthetic-wavelength-based dual-comb interferometry for fast and precise absolute distance measurement," Opt. Express **26**, 5747–5757 (2018).
10. L. Yan, J. Xie, B. Chen, *et al.*, "Absolute distance measurement using laser interferometric wavelength leverage with a dynamic-sideband-locked synthetic wavelength generation," Opt. Express **29**, 8344–8357 (2021).
11. N. Schuhler, Y. Salvadé, S. Lévêque, *et al.*, "Frequency-comb-referenced two-wavelength source for absolute distance measurement," Opt. Lett. **31**, 3101–3103 (2006).
12. G. Wang, Y.-S. Jang, S. Hyun, *et al.*, "Absolute positioning by multi-wavelength interferometry referenced to the frequency comb of a femtosecond laser," Opt. Express **23**, 9121–9129 (2015).
13. Y.-S. Jang, G. Wang, S. Hyun, *et al.*, "Comb-referenced laser distance interferometer for industrial nanotechnology," Sci. Rep. **6**, 31770 (2016).
14. R. Dändliker, R. Thalmann, and D. Prongué, "Two-wavelength laser interferometry using superheterodyne detection," Opt. Lett. **13**, 339–341 (1988).
15. C. C. Williams and H. K. Wickramasinghe, "Absolute optical ranging with 200-nm resolution," Opt. Lett. **14**, 542–544 (1989).
16. R. W. Fox, B. R. Washburn, N. R. Newbury, *et al.*, "Wavelength references for interferometry in air," Appl. Opt. **44**, 7793–7801 (2005).
17. K. Minoshima and H. Matsumoto, "High-accuracy measurement of 240-m distance in an optical tunnel by use of a compact femtosecond laser," Appl. Opt. **39**, 5512–5517 (2000).
18. K. Määttä, J. Kostamovaara, and R. Myllylä, "Profiling of hot surfaces by pulsed time-of-flight laser range finder techniques," Appl. Opt. **32**, 5334–5347 (1993).
19. F. Dill, "Gallium arsenide injection laser," in *IEEE International Solid-State Circuits Conference*, Digest of Technical Papers (1963), pp. 110–111.
20. T. Udem, R. Holzwarth, and T. W. Hänsch, "Optical frequency metrology," Nature **416**, 233–237 (2002).
21. S.-W. Kim, "Combs rule," Nat. Photonics **3**, 313–314 (2009).
22. S. A. Diddams, "The evolving optical frequency comb [invited]," J. Opt. Soc. Am. B **27**, B51–B62 (2010).
23. T. Fortier and E. Baumann, "20 years of developments in optical frequency comb technology and applications," Commun. Phys. **2**, 153 (2019).
24. N. R. Newbury, "Searching for applications with a fine-tooth comb," Nat. Photonics **5**, 186–188 (2011).

25. T. Udem, J. Reichert, R. Holzwarth, *et al.*, "Absolute optical frequency measurement of the cesium D1 line with a mode-locked laser," Phys. Rev. Lett. **82**, 3568–3571 (1999).

26. D. J. Jones, S. A. Diddams, J. K. Ranka, *et al.*, "Carrier-envelope phase control of femtosecond mode-locked lasers and direct optical frequency synthesis," Science **288**, 635–639 (2000).

27. S. A. van den Berg, S. van Eldik, and N. Bhattacharya, "Mode-resolved frequency comb interferometry for high-accuracy long distance measurement," Sci. Rep. **5**, 14661 (2015).

28. K.-N. Joo and S.-W. Kim, "Absolute distance measurement by dispersive interferometry using a femtosecond pulse laser," Opt. Express **14**, 5954–5960 (2006).

29. M. Cui, M. G. Zeitouny, N. Bhattacharya, *et al.*, "Long distance measurement with femtosecond pulses using a dispersive interferometer," Opt. Express **19**, 6549–6562 (2011).

30. J. Wang, Z. Lu, W. Wang, *et al.*, "Long-distance ranging with high precision using a soliton microcomb," Photon. Res. **8**, 1964–1972 (2020).

31. S. A. van den Berg, S. T. Persijn, G. J. P. Kok, *et al.*, "Many-wavelength interferometry with thousands of lasers for absolute distance measurement," Phys. Rev. Lett. **108**, 183901 (2012).

32. J. Lee, Y.-J. Kim, K. Lee, *et al.*, "Time-of-flight measurement with femtosecond light pulses," Nat. Photonics **4**, 716–720 (2010).

33. D. Wei, S. Takahashi, K. Takamasu, *et al.*, "Time-of-flight method using multiple pulse train interference as a time recorder," Opt. Express **19**, 4881–4889 (2011).

34. J. Ye, "Absolute measurement of a long, arbitrary distance to less than an optical fringe," Opt. Lett. **29**, 1153–1155 (2004).

35. Y.-S. Jang and S.-W. Kim, "Distance measurements using mode-locked lasers: a review," Nanomanuf. Metrol. **1**, 131–147 (2018).

36. H. Zhang, H. Wei, X. Wu, *et al.*, "Absolute distance measurement by dual-comb nonlinear asynchronous optical sampling," Opt. Express **22**, 6597–6604 (2014).

37. G. Wu, S. Xiong, K. Ni, *et al.*, "Parameter optimization of a dual-comb ranging system by using a numerical simulation method," Opt. Express **23**, 32044–32053 (2015).

38. P. Trocha, M. Karpov, D. Ganin, *et al.*, "Ultrafast optical ranging using microresonator soliton frequency combs," Science **359**, 887–891 (2018).

39. H. Shi, Y. Song, F. Liang, *et al.*, "Effect of timing jitter on time-of-flight distance measurements using dual femtosecond lasers," Opt. Express **23**, 14057–14069 (2015).

40. I. Coddington, W. C. Swann, L. Nenadovic, *et al.*, "Rapid and precise absolute distance measurements at long range," Nat. Photonics **3**, 351–356 (2009).

41. E. D. Caldwell, L. C. Sinclair, N. R. Newbury, *et al.*, "The time-programmable frequency comb and its use in quantum-limited ranging," Nature **610**, 667–673 (2022).

42. T. Mitchell, J. Sun, and D. T. Reid, "Dynamic measurements at up to 130-kHz sampling rates using Ti:sapphire dual-comb distance metrology," Opt. Express **29**, 42119–42126 (2021).

43. J. Azaña and M. A. Muriel, "Real-time optical spectrum analysis based on the time-space duality in chirped fiber gratings," IEEE J. Quantum Electron. **36**, 517–526 (2000).

44. B. Li, J. Xing, D. Kwon, *et al.*, "Bidirectional mode-locked all-normal dispersion fiber laser," Optica **7**, 961–964 (2020).

45. T. Ideguchi, T. Nakamura, Y. Kobayashi, *et al.*, "Kerr-lens mode-locked bidirectional dual-comb ring laser for broadband dual-comb spectroscopy," Optica **3**, 748–753 (2016).

46. N. Prakash, S.-W. Huang, and B. Li, "Relative timing jitter in a counter-propagating all-normal dispersion dual-comb fiber laser," Optica **9**, 717–723 (2022).

47. S. M. Link, A. Klenner, M. Mangold, *et al.*, "Dual-comb modelocked laser," Opt. Express **23**, 5521–5531 (2015).